

HIGH-ORDER DISCONTINUOUS GALERKIN SOLUTION OF THE RANS AND EXPLICIT ALGEBRAIC REYNOLDS STRESS k - ω EQUATIONS IN TURBOMACHINERY FLOWS

*F. Bassi*¹ - *L. Botti*¹ - *A. Colombo*¹ - *N. Franchina*¹
*A. Ghidoni*² - *A. Nigro*³ - *S. Rebay*²

¹ Department of Engineering, University of Bergamo, Dalmine (BG), Italy
email: {francesco.bassi,lorenzo.botti,alessandro.colombo}@unibg.it

² Department of Mechanical and Industrial Engineering, University of Brescia, Brescia, Italy
email: {antonio.ghidoni,stefano.rebay@ing.unibs.it}

³ Department of Mechanic, University of Calabria, Arcavata di Rende (CS), Italy
email: anigro@unical.it

ABSTRACT

The objective of this work is to show the effectiveness of a high-order accurate Discontinuous Galerkin (DG) space discretization in the numerical simulation of the 3D compressible turbulent flow through a turbine cascade (MTU T106A). The turbulent flow field is computed by means of the Reynolds Averaged Navier-Stokes (RANS) equations with closure provided by the k - ω turbulence model and an Explicit Algebraic Reynolds Stress Model (EARSM). Results obtained with both models will be analysed and compared.

NOMENCLATURE

ρ density
 u_i velocity components
 e_0 total energy
 h_0 total enthalpy
 k turbulent kinetic energy
 ω specific turbulent dissipation rate
 p pressure
 q_j heat flux vector
 $\hat{\tau}_{ij}$ total stress tensor
 \mathcal{P} production terms
 $\bar{\mu}_t$ eddy viscosity
 γ ratio of gas specific heats
Pr molecular Prandtl number
Pr_t turbulent Prandtl number
 S_{ij} mean strain-rate tensor
 Ω_{ij} rate-of-rotation tensor
 τ_{ij} turbulent stress tensor
 a_{ij} anisotropy tensor
 $a_{ij}^{(ex)}$ extra anisotropy tensor
 \mathbf{u} vector of variables
 s source term
 \mathbf{F}_c inviscid flux vector
 \mathbf{F}_v viscous flux vector
 \mathbf{v} test function
 Ω computational domain

$\partial\Omega$ domain boundary
 \mathcal{T}_h computational mesh
 T grid element
 \mathcal{F}_h set of boundary and internal faces
 \mathbf{r} lifting operator
 $\hat{\mathbf{F}}$ numerical flux function
 η_F penalty parameter
 \mathbf{U} global vector of unknown degrees of freedom
 \mathbf{M} global block diagonal mass matrix
 \mathbf{R} residuals vector
 \mathbb{P}^n solution polynomial approximation of degree n
 $\alpha_{1,b}, \alpha_{2,b}$ inlet/outlet blade angle
 c, c_{ax} chord, axial chord
 s pitch
 α_1 inlet flow angle
 p_{01} inlet total pressure
 p_0 total pressure
 Tu_1 inlet turbulence intensity
 $M_{2,is}$ outflow isentropic Mach number
 $Re_{2,is}$ Reynolds number based on downstream isentropic conditions and blade chord
 C_p pressure coefficient
 y^+ non dimensional wall distance

INTRODUCTION

Numerical simulation has become an important tool in almost all sectors of fluids engineering. This evolution has been possible due to the ever-increasing computational power, but is foremost motivated by the increasing requirements and regulations in terms of energy efficiency and environmental impact. Nowadays most computational fluid dynamics (CFD) tools are based on second-order accurate Finite Volume (FV) methods. Due to the required level of resolution and the need of analyse ever more complex geometries and flows, there is a growing concern that state-of-the-art FV technology requires, and will continue to require, too extensive computational resources. The requirement for high resolution hence naturally leads to consider methods which have a higher order of accuracy, such as Discontinuous Galerkin (DG) methods (Bassi et al., 2005).

Recently developed high-order methods have demonstrated a huge potential, which has not yet been exploited to fulfil industrial requirements. In fact high-order solvers are currently able to solve 3D turbulent flow problems (Bassi et al., 2010a, 2011a) by means of the solution of the Reynolds Average Navier-Stokes (RANS) and $k-\omega$ turbulence model equations, even if they are either extremely memory consuming and/or CPU intensive.

Usually, standard CFD codes adopt the Boussinesq hypothesis that assumes Reynolds stress is linearly related to the mean flow strain rate tensor. However such hypothesis shows limitations in the prediction of some flow features, such as for example the secondary flows that develop at wall junctions (Menter et al., 2009). Several authors have suggested to replace the Boussinesq linear constitutive law with a non-linear relation to enhance the prediction capabilities.

The solution of the RANS and explicit algebraic Reynolds stress $k-\omega$ equations by means of a high-order accurate method can represent a trade-off between standard RANS plus two equations turbulence models simulations and more accurate and intensive simulations (e.g. DES, LES, DNS).

The objective of this work is to show the effectiveness of a high-order accurate DG space discretization in the numerical simulation of the 3D compressible turbulent flow through the T106A turbine cascade. In particular, the feasibility of accurate simulations of such complex flows on very

coarse grids by resorting to a sufficiently high-order accurate DG space discretization is demonstrated. Furthermore a comparison of the computed flow field obtained by means of the RANS equations with closure provided by the k - ω turbulence model (Bassi et al., 2011a) and the Explicit Algebraic Reynolds Stress Model (EARSM) of Wallin and Johansson (2000) is shown.

GOVERNING EQUATIONS

The governing equations can be written as

$$\frac{\partial \rho}{\partial t} + \frac{\partial}{\partial x_j}(\rho u_j) = 0, \quad (1)$$

$$\frac{\partial}{\partial t}(\rho u_i) + \frac{\partial}{\partial x_j}(\rho u_j u_i) = -\frac{\partial p}{\partial x_i} + \frac{\partial \hat{\tau}_{ji}}{\partial x_j}, \quad (2)$$

$$\frac{\partial}{\partial t}(\rho e_0) + \frac{\partial}{\partial x_j}(\rho u_j h_0) = \frac{\partial}{\partial x_j} [u_i \hat{\tau}_{ij} - q_j] - \mathcal{P}_k + \beta^* \rho \bar{k} e^{\tilde{\omega}}, \quad (3)$$

$$\frac{\partial}{\partial t}(\rho k) + \frac{\partial}{\partial x_j}(\rho u_j k) = \frac{\partial}{\partial x_j} \left[(\mu + \sigma^* \bar{\mu}_t) \frac{\partial k}{\partial x_j} \right] + \mathcal{P}_k - \beta^* \rho \bar{k} e^{\tilde{\omega}}, \quad (4)$$

$$\begin{aligned} \frac{\partial}{\partial t}(\rho \tilde{\omega}) + \frac{\partial}{\partial x_j}(\rho u_j \tilde{\omega}) &= \frac{\partial}{\partial x_j} \left[(\mu + \sigma \bar{\mu}_t) \frac{\partial \tilde{\omega}}{\partial x_j} \right] + \mathcal{P}_\omega - \beta \rho e^{\tilde{\omega}} \\ &+ (\mu + \sigma \bar{\mu}_t) \frac{\partial \tilde{\omega}}{\partial x_k} \frac{\partial \tilde{\omega}}{\partial x_k} + \sigma_d \frac{\rho}{e^{\tilde{\omega}}} \max \left(\frac{\partial k}{\partial x_k} \frac{\partial \tilde{\omega}}{\partial x_k}; 0 \right), \end{aligned} \quad (5)$$

where the pressure, the total stress tensor, the heat flux vector, the production terms \mathcal{P}_k and \mathcal{P}_ω and the limited value of turbulent kinetic energy \bar{k} are defined as

$$p = (\gamma - 1) \rho (e_0 - u_k u_k / 2), \quad (6)$$

$$\hat{\tau}_{ij} = 2\mu S_{ij} + \tau_{ij}, \quad (7)$$

$$q_j = - \left(\frac{\mu}{\text{Pr}} + \frac{\bar{\mu}_t}{\text{Pr}_t} \right) \frac{\partial h}{\partial x_j}, \quad (8)$$

$$\mathcal{P}_k = \tau_{ij} \frac{\partial u_i}{\partial x_j}, \quad \mathcal{P}_\omega = \alpha \frac{\tau_{ij}}{\bar{k}} \frac{\partial u_i}{\partial x_j}, \quad (9)$$

$$\bar{k} = \max(0, k). \quad (10)$$

Here γ is the ratio of gas specific heats, Pr and Pr_t are the molecular and turbulent Prandtl numbers and

$$S_{ij} = \frac{1}{2} \left(\frac{\partial u_i}{\partial x_j} + \frac{\partial u_j}{\partial x_i} \right) - \frac{1}{3} \frac{\partial u_k}{\partial x_k} \delta_{ij}, \quad \Omega_{ij} = \frac{1}{2} \left(\frac{\partial u_i}{\partial x_j} - \frac{\partial u_j}{\partial x_i} \right), \quad (11)$$

are the mean strain-rate and the rate-of-rotation tensors. The closure coefficients $\alpha, \alpha^*, \beta, \beta^*, \sigma, \sigma^*, \sigma_d$ are those of the high- or low-Reynolds number k - ω model of Wilcox (1993). Notice that Eq. (5) of the k - ω turbulence model is not in standard form since the variable $\tilde{\omega} = \log \omega$ is used instead of ω , as explained in Bassi et al. (2005). According to Wallin and Johansson (2000), the constitutive relation for the turbulent stress tensor can be written as

$$\frac{\tau_{ij}}{\rho \bar{k}} = -\frac{\overline{u_i u_j}}{\bar{k}} = -\alpha^* a_{ij} - \frac{2}{3} \delta_{ij} = \alpha^* \left(2C_\mu \tau S_{ij} - a_{ij}^{(\text{ex})} \right) - \frac{2}{3} \delta_{ij}, \quad (12)$$

where, for ease of implementation, the anisotropy tensor a_{ij} has been split in a linear part and a non-linear extra anisotropy contribution. The time scale τ and the variable coefficient C_μ are given by

$$\tau = \frac{1}{\beta^* e^{\tilde{\omega}}}, \quad C_\mu = -\frac{1}{2}(\beta_1 + II_\Omega \beta_6). \quad (13)$$

The time scale τ does not include the near-wall lower bound, based on the Kolmogorov time scale, usually employed in k - ϵ implementations of EARSM. This limitation is actually provided by the finite value of ω set at wall. The eddy viscosity $\bar{\mu}_t$ and the extra anisotropy tensor $a_{ij}^{(\text{ex})}$ are given by

$$\bar{\mu}_t = \alpha^* C_\mu \tau \rho \bar{k}, \quad (14)$$

$$\begin{aligned} a_{ij}^{(\text{ex})} = & \beta_3 \tau^2 \left(\Omega_{ik} \Omega_{kj} - \frac{1}{3} II_\Omega \delta_{ij} \right) \\ & + \beta_4 \tau^2 (S_{ik} \Omega_{kj} - \Omega_{ik} S_{kj}) \\ & + \beta_6 \tau^3 \left(S_{ik} \Omega_{kl} \Omega_{lj} + \Omega_{ik} \Omega_{kl} S_{lj} - II_\Omega S_{ij} - \frac{2}{3} IV \delta_{ij} \right) \\ & + \beta_9 \tau^4 (\Omega_{ik} S_{kl} \Omega_{lm} \Omega_{mj} + \Omega_{ik} \Omega_{kl} S_{lm} \Omega_{mj}), \end{aligned} \quad (15)$$

where the coefficients $\beta_{i \in \{1,3,4,6,9\}}$ are functions of the invariants II_S , II_Ω and IV

$$II_S = \text{tr}\{\mathbf{S}^2\}, \quad II_\Omega = \text{tr}\{\mathbf{\Omega}^2\}, \quad IV = \text{tr}\{\mathbf{S}\mathbf{\Omega}^2\}. \quad (16)$$

DG SPACE DISCRETIZATION

RANS and turbulence model/EARSM equations can be written in compact form as

$$\frac{\partial \mathbf{u}}{\partial t} + \nabla \cdot \mathbf{F}_c(\mathbf{u}) + \nabla \cdot \mathbf{F}_v(\mathbf{u}, \nabla \mathbf{u}) + \mathbf{s}(\mathbf{u}, \nabla \mathbf{u}) = \mathbf{0}, \quad (17)$$

where \mathbf{u} and \mathbf{s} are the vectors of the m variables and source terms, and $\mathbf{F}_c, \mathbf{F}_v \in \mathbb{R}^m \otimes \mathbb{R}^d$ are defined as the arrays of the inviscid and viscous flux vectors. A weak formulation of the RANS equations is obtained multiplying each scalar conservation law in Eq. (17) by an arbitrary smooth test function $v_j \in \mathbf{v}$, $1 \leq j \leq m$, and integrating by parts, that is

$$\int_\Omega v_j \frac{\partial u_j}{\partial t} d\mathbf{x} - \int_\Omega \nabla v_j \cdot \mathbf{F}_j(\mathbf{u}, \nabla \mathbf{u}) d\mathbf{x} + \int_{\partial\Omega} v_j \mathbf{F}_j(\mathbf{u}, \nabla \mathbf{u}) \cdot \mathbf{n} d\sigma + \int_\Omega v_j \mathbf{s}_j(\mathbf{u}, \nabla \mathbf{u}) d\mathbf{x} = 0, \quad (18)$$

where \mathbf{F}_j is the sum of the inviscid and viscous flux vectors of the j -th equation, Ω is the domain where the solution is to be computed, $\partial\Omega$ is its boundary, and \mathbf{n} is the unit outward normal vector to the boundary.

The DG discretization of Eq. (18) is constructed on a mesh \mathcal{T}_h , which consists on a set of non-overlapping elements T . The function \mathbf{u} and \mathbf{v} are approximated on \mathcal{T}_h as piecewise polynomial functions \mathbf{u}_h and \mathbf{v}_h which are in general discontinuous on element interfaces. The discontinuous approximation of the numerical solution requires to introduce a specific treatment of the inviscid and viscous interface fluxes. In order to ensure conservation and correctly account for wave propagation the former is based on the Godunov flux computed with an exact Riemann solver or, alternatively, on the van Leer-Hänel flux-splitting scheme (Hänel et al., 1987). For the latter the BR2 scheme has been employed, proposed in Bassi et al. (1997) and theoretically analyzed in Brezzi et al. (2000); Arnold et al. (2002).

Accounting for these aspects, the DG formulation of the compressible RANS and k - ω /EARSM equations consists in seeking \mathbf{u}_h such that

$$\begin{aligned} \sum_{T \in \mathcal{T}_h} \int_T v_{h,j} \frac{\partial u_{h,j}}{\partial t} d\mathbf{x} - \sum_{T \in \mathcal{T}_h} \int_T \nabla_h v_{h,j} \cdot \mathbf{F}_j(\mathbf{u}_h, \nabla_h \mathbf{u}_h + \mathbf{r}(\llbracket \mathbf{u}_h \rrbracket)) d\mathbf{x} \\ + \sum_{F \in \mathcal{F}_h} \int_F \llbracket v_{h,j} \rrbracket \cdot \hat{\mathbf{F}}_j(\mathbf{u}_h^\pm, (\nabla_h \mathbf{u}_h + \eta_F \mathbf{r}_F(\llbracket \mathbf{u}_h \rrbracket))^\pm) d\sigma \\ + \sum_{T \in \mathcal{T}_h} \int_T v_{h,j} \mathbf{s}_j(\mathbf{u}_h, \nabla_h \mathbf{u}_h + \mathbf{r}(\llbracket \mathbf{u}_h \rrbracket)) d\mathbf{x} = 0 \end{aligned} \quad (19)$$

$\forall \mathbf{v}_h,$

where \mathcal{F}_h is the set of boundary and internal faces, $\hat{\mathbf{F}}$ the numerical flux function, $\llbracket \cdot \rrbracket$ the jump operator, and \mathbf{r} the lifting operator. In order to ensure the stability of the BR2 discretization, theory predicts that the penalty parameter η_F in Eq. (19) has to be set larger than the number of faces of each element (Brezzi et al., 2000; Arnold et al., 2002).

The DG space discretization of Eq. (19) results in the following system of (nonlinear) ODEs in time

$$\mathbf{M} \frac{d\mathbf{U}}{dt} + \mathbf{R}(\mathbf{U}) = \mathbf{0}, \quad (20)$$

where \mathbf{U} is the global vector of unknown degrees of freedom, \mathbf{M} is a global block diagonal matrix (\mathbf{M} reduces to the identity matrix due to the use of orthonormal basis functions) and $\mathbf{R}(\mathbf{U})$ is the vector of residuals.

In the case of steady state computations the semi-discrete problem in Eq. (19) is discretized in time by means of the classical backward Euler scheme coupled with the pseudo-transient continuation strategy proposed in Bassi et al. (2010a). The resulting linear system is solved at each time step by means of the matrix-explicit or the matrix-free GMRES algorithm. Linear algebra and parallelization are handled through PETSc library (Balay et al., 2001).

RESULTS

The purpose of this section is to demonstrate the performance of the DG method in the computation of the turbulent flow through a well known turbine cascade, and in particular the potential of this high-order method to resolve complex turbulent flow features on a very coarse grid. This section also discusses the effectiveness and limitations of the k - ω turbulence model and EARSM in the prediction of the flow field. Starting from the linear part of the Reynolds stress tensor formulation of Eq. (12), we evaluate the influence of the non-linear terms of EARSM on the solutions. In the following, the notation EARSM $_x$ means EARSM including anisotropy terms up to the x -th degree.

The test case chosen for the simulations is the T106A turbine cascade. It is a low-pressure turbine cascade designed by MTU Aero Engines, which has been extensively investigated in experimental and computational studies (Hoheisel, 1981; Stieger and Hodson, 2004, 2005; Lodefier and Dick, 2005; Bassi et al., 2012). The main geometrical parameters of the cascade are given in Tab. 1.

An adiabatic wall boundary condition is imposed on the blade surface and end-walls. At inflow, the total temperature, total pressure, flow angle $\alpha_1 = 37.7^\circ$ and turbulence intensity $Tu_1 = 4.0\%$ are prescribed while at outflow the static pressure corresponding to an isentropic Mach number $M_{2,is} = 0.59$ is set. The Reynolds number based on the downstream isentropic conditions and on the blade chord is $Re_{2,is} = 500000$.

Computations have been performed with the standard k - ω model and with EARSM1 \rightarrow 3 up to \mathbb{P}^3 polynomial approximation on a grid composed of 43200 hexahedral elements, see Figure 1. The

Table 1: Geometrical parameters of T106A turbine cascade

$\alpha_{1,b}$	inlet angle	37.7°
$\alpha_{2,b}$	outlet angle	-63.2°
c	chord	0.1 m
s	pitch	0.0799 m
s/c	pitch to chord ratio	0.799 m

geometry has been represented with bi-quadratic faces since for DG space approximation a curved approximation at the wall is mandatory in order to obtain accurate results (Bassi and Rebay, 1997). Wall-normal height of elements adjacent to the wall corresponds to $y^+ \approx 20$. It is considerably greater than that typically required by second-order accurate FV simulations of turbulent flows ($y^+ \approx 1$ without wall functions) but can be adopted for higher-order DG approximations (Bassi et al., 2005). Notice that the y^+ value chosen for the mesh is appropriate only for the high-order solutions, but it is not changed in the lower-order computations because their solutions are just intended for the initialization of the higher-order computations.

All the computations have been run in parallel (132 cores/11 processors for $k-\omega$ and EARSM1, 264 cores/22 processors for EARSM2 \rightarrow 3), initializing the \mathbb{P}^0 solution from uniform outlet flow conditions and the higher-order solutions from the lower-order ones. At the moment, a comparison in term of computational time between FV and DG schemes would require an in-depth analysis and the use of an engineering convergence criterion (the converged solution is now reached when the L^2 norm of the residuals is below 10^{-8}). However it is clear that FV computational efficiency is still greater, even if DG methods show a substantial room for improvement. For this reason research effort has been recently devoted to devise more efficient computational strategies, both for the construction of DG space discretization operators and for the integration in time of the space discretized DG equations (see e.g. Bassi et al. (2011b, 2009, 2010b)).

Figure 2 and 3 show stream traces and skin-friction lines patterns near the end-wall obtained with the EARSM3 model and \mathbb{P}^3 solution, which displays some vortical structures characterizing the flow field. In particular it can be observed the horse-shoe vortex, originating near the blade leading edge. The pressure side leg of the horse-shoe vortex is driven along the separation line across the passage from the leading edge to the adjacent blade suction side and merges in the passage vortex. In Figure 4 the midspan pressure coefficient C_p curves of the $k-\omega$ and EARSM1 \rightarrow 3 are displayed, showing a good agreement with the experimental data (Hoheisel, 1981). There is a small difference in the rear part of the suction side, because the laminar separation bubble is not predicted, due to the lack of a transition model. As expected, at midspan the models do not show any difference in the computed flow field.

In order to asses the effectiveness of the EARSM, flow features near the end-walls are now analyzed. In Figure 5 turbulence intensity and total pressure contours at the junction between the blade suction side and the end-wall are depicted on a plane normal to the axial direction ($x/c_{ax} = 0.93$). The turbulence distribution of the EARSM1 \rightarrow 3 results are more sharply defined and better resolved in a vortex-like structure when compared to the standard $k-\omega$ model. In particular the passage vortex and the corner vortex at the junction are better resolved with EARSM. Figure 6 shows same contours on a different plane ($x/c_{ax} = 1.04$), which is just after the blade trailing edge. Also in this case the vortical structures are better resolved by using EARSM models. Notice that corner vortex is captured only by using the EARSM models, as shown by the total pressure contours. In Figure 7 the M_z isolines and the stream traces in a plane normal to the axial direction ($x/c_{ax} = 1.447$) are depicted. It can be observed the different shape and intensity of the vortex. In particular vortices

obtained with ERASM2-3 are characterized by greater velocity gradients. Differences between models are now analyzed in terms of total pressure distributions, $p_0/p_{0,1}$ (normalized with respect to the inflow value), along the pitch-wise direction at different blade heights and distance from the trailing edge. In particular in Figure 8 the total pressure distribution at $x/c_{ax} = 1.187$ (top), $x/c_{ax} = 1.332$ (central) and $x/c_{ax} = 1.447$ for a blade height $z/h = 0.33\%$ (left) and $z/h = 4.67\%$ (right) is shown. Notice that at $z/h = 4.67\%$ (right column) the total pressure distributions predicted by the models are similar. There are just small differences in the distribution inside the wake and in term of amplitude of the wake (the wake predicted by EARSMS2→3 models is greater, probably due to a better resolution of the passage vortex). Moving away from the trailing edge (right, top → bottom), all models, as expected, predict an increasing of the vortices amplitude. At the wake interfaces there are some nonphysical oscillations above unit of $p_0/p_{0,1}$. This phenomenon can be explained by the low resolution of the blade leading edge, which produce an oscillations in the total pressure, which is advected downstream due to the low diffusion property of the DG schemes. Decreasing the distance from the end-wall, $z/h = 0.33\%$ (left column), total pressure distributions are instead different. In particular near the trailing edge ($x/c_{ax} = 1.187$) $k-\omega$ model predicts a wake characterized by higher total pressure losses and greater amplitude. Total pressure losses between adjacent wakes are instead lower for the $k-\omega$ model, due probably to the corner vortices, which are not captured very well. Notice that there is no appreciable differences between EARSMS2→3 total pressure distribution curves, meaning that in both cases a “converged” solution has been reached. Moving away from the trailing edge (left, top → bottom), differences in the wakes predicted by $k-\omega$ and EARSMS become greater, implying a different evolution of the vortex, as already observed in Figure 7.

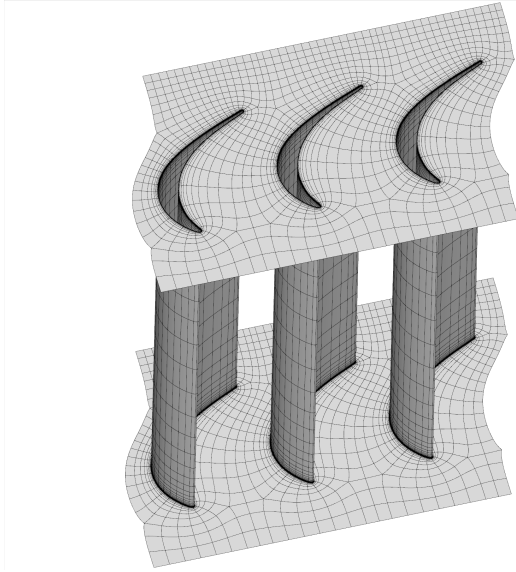


Figure 1: Computational grid, 43200 hexahedral elements with bi-quadratic faces, Wall surfaces

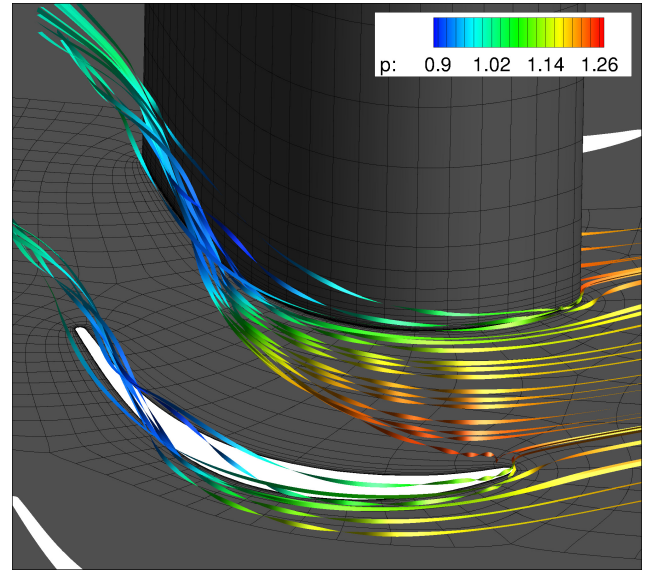


Figure 2: Stream traces near the end-wall, EARSMS3, \mathbb{P}^3 solution

CONCLUSIONS

An implicit high-order DG solver for the RANS equations coupled with the standard $k-\omega$ and the EARSMS $k-\omega$ turbulence models has been presented and applied to compute the subsonic flow through the MTU T106A turbine cascade.

The computational results have been compared in order to assess the benefits of the improved Reynolds stress modelization provided by the EARSMS $k-\omega$ model. As expected, this model provided better resolution of rotational flow features taking place close to the end-walls and at the

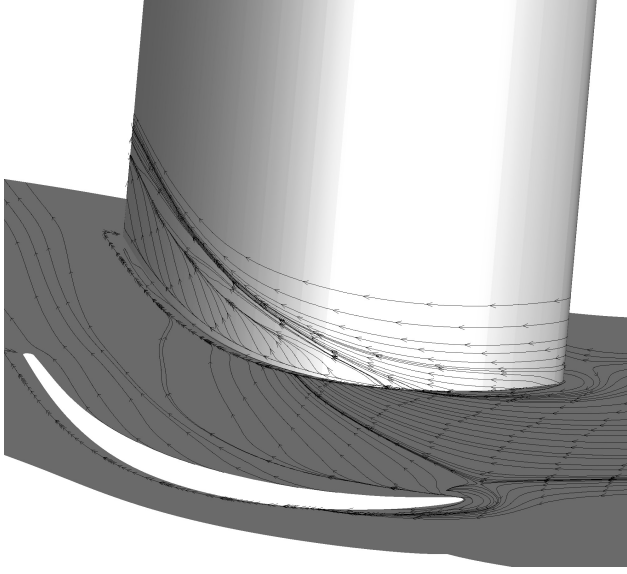


Figure 3: Skin-friction lines near the end-wall, EARSM3, \mathbb{P}^3 solution

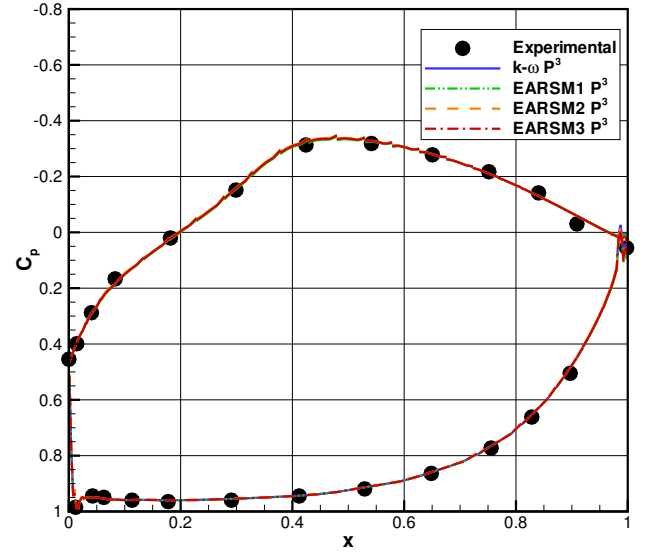


Figure 4: Pressure coefficient distribution at midspan, $k-\omega$ and EARSM1 \rightarrow 3, \mathbb{P}^3 solution

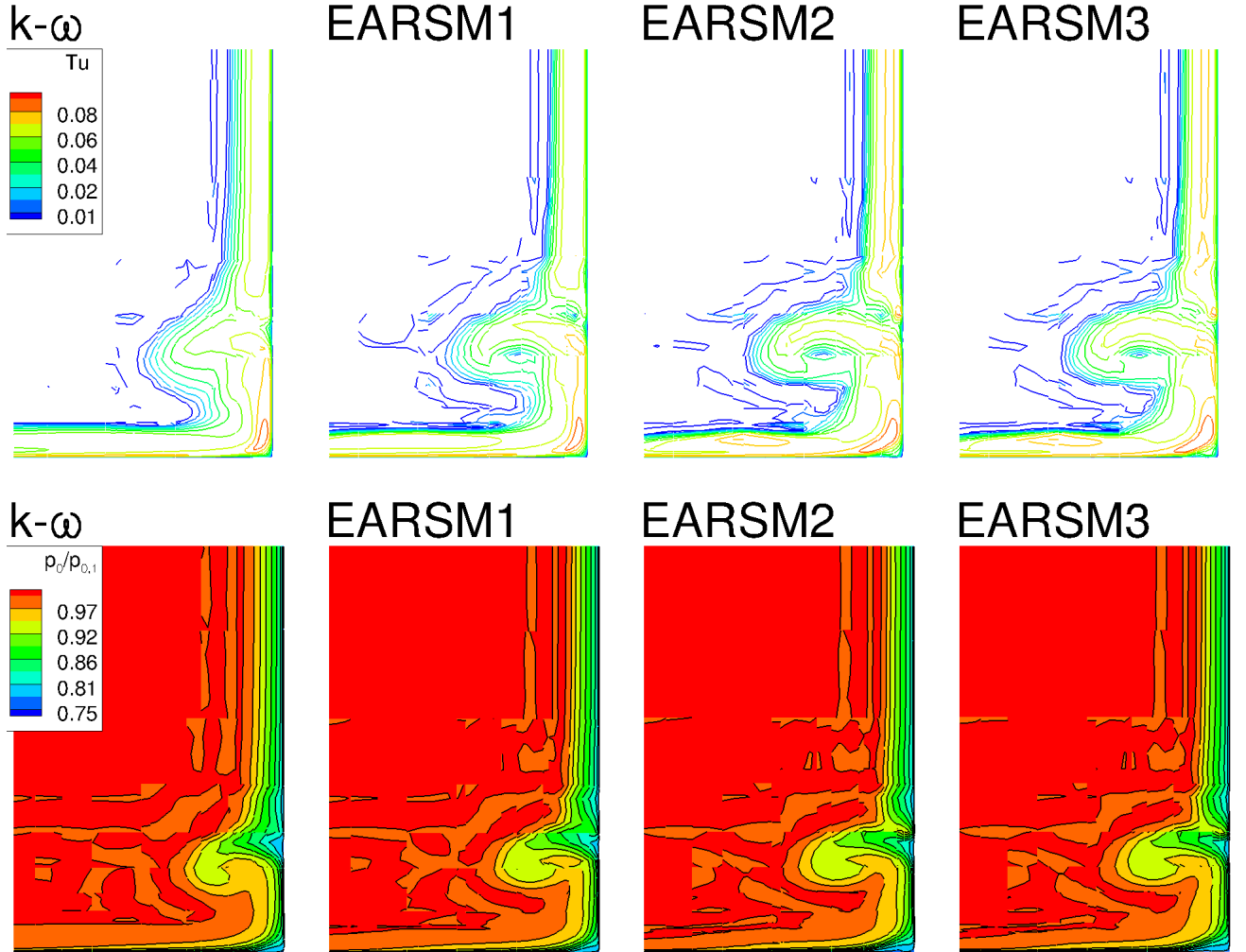


Figure 5: Turbulence intensity (top) and total pressure (bottom) contours at junction between end-wall and suction side on a plane normal to the axial direction ($x/c_{ax} = 0.93$)

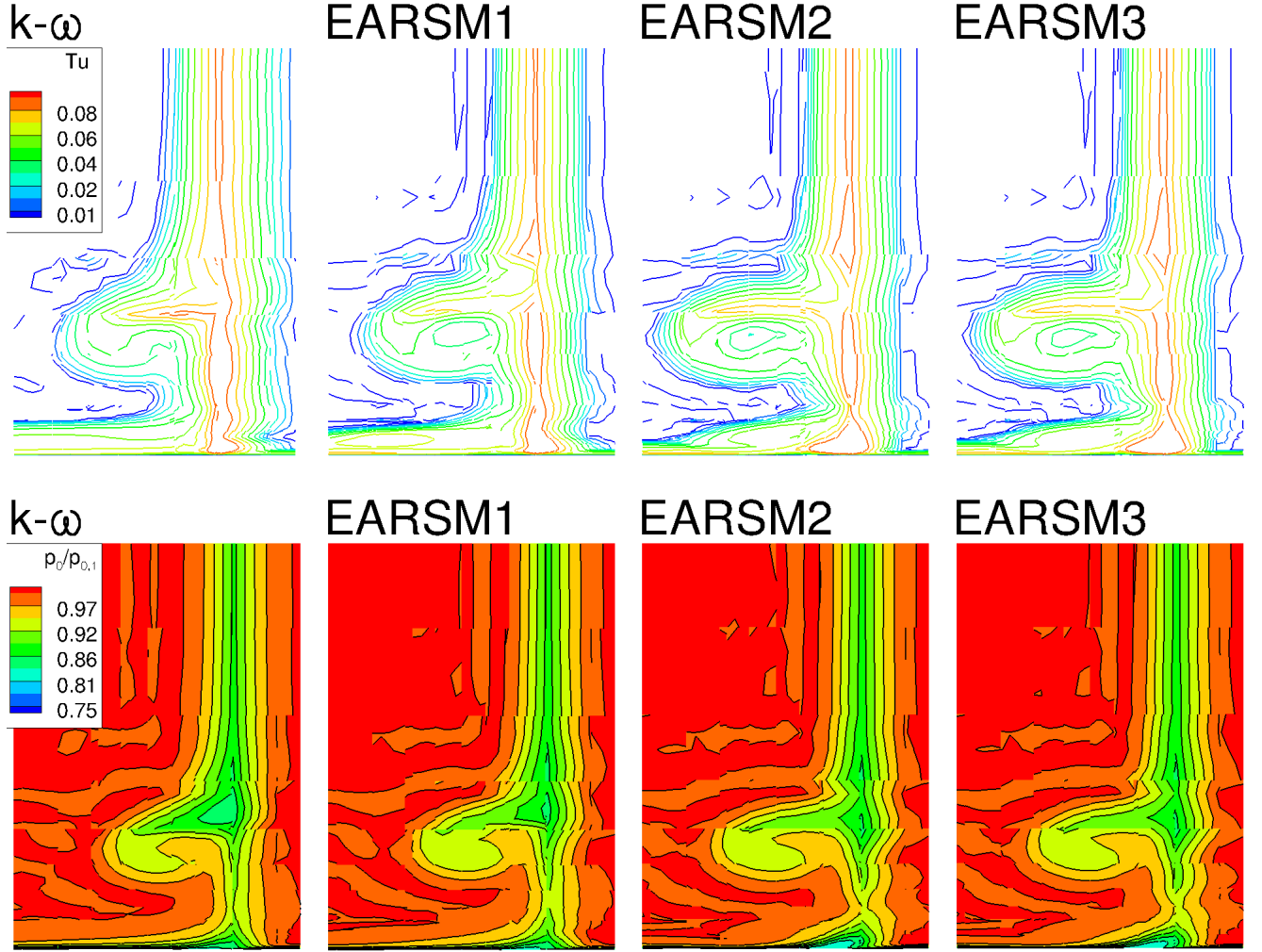


Figure 6: Turbulence intensity (top) and total pressure (bottom) contours at junction between end-wall and suction side on a plane normal to the axial direction ($x/c_{ax} = 1.04$)

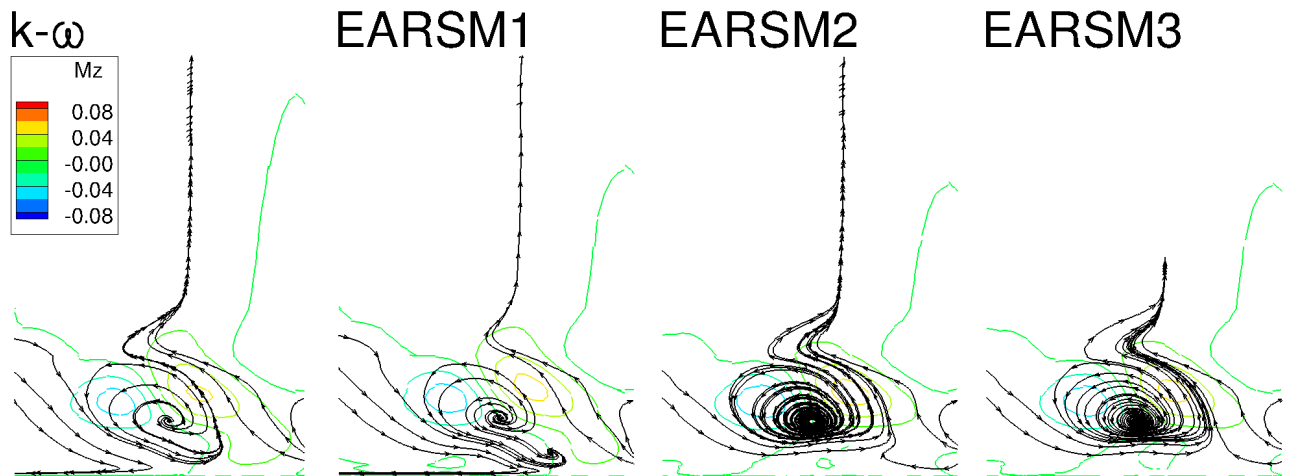


Figure 7: M_z isolines and stream traces on a plane normal to the axial direction ($x/c_{ax} = 1.447$), $k-\omega$ and EARS1→3, \mathbb{P}^3 solution

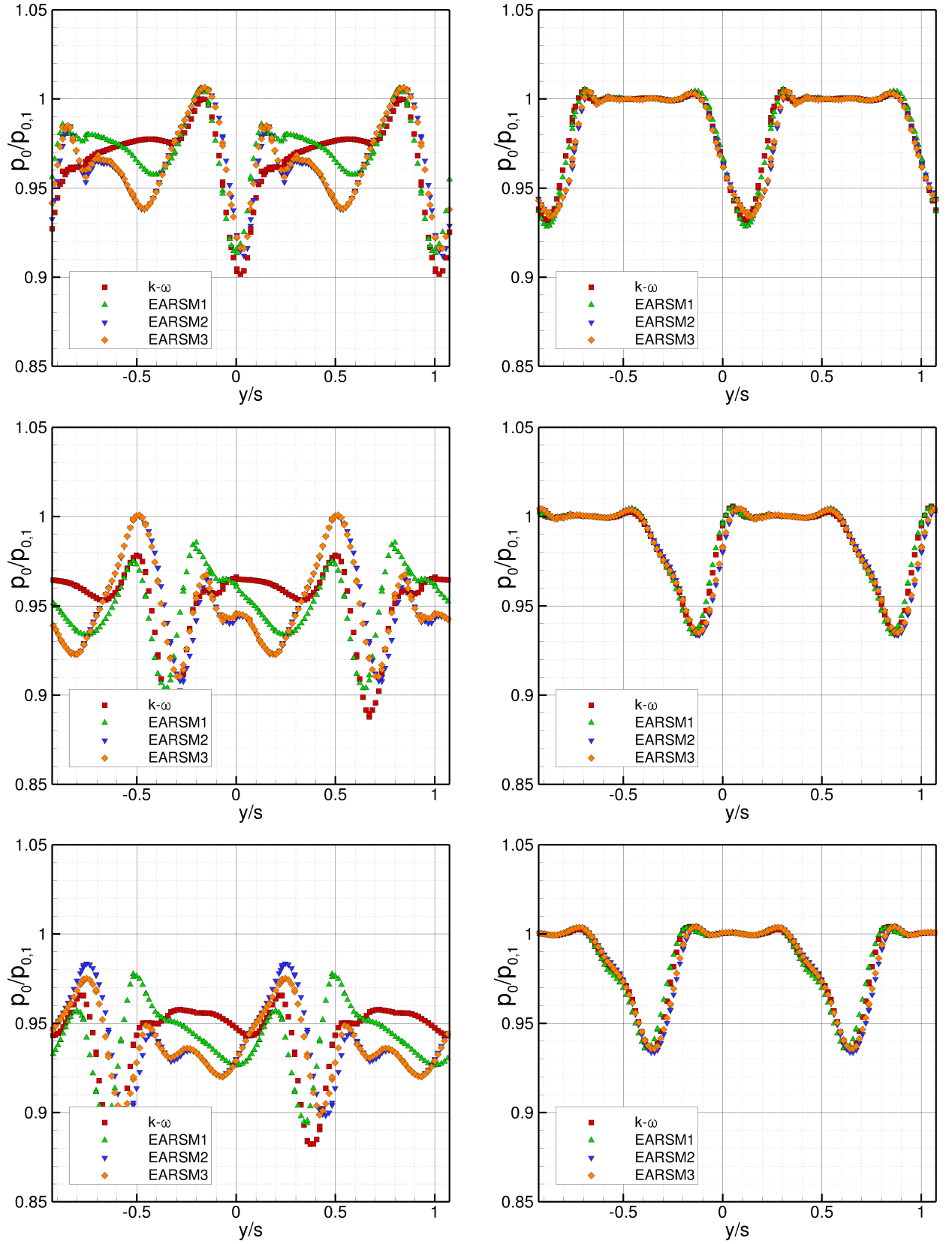


Figure 8: Pitch-wise total pressure distribution at $x/c_{ax} = 1.187$ (top), $x/c_{ax} = 1.332$ (central) and $x/c_{ax} = 1.447$ for a blade height $z/h = 0.33\%$ (left) and $z/h = 4.67\%$ (right), $k-\omega$ and EARSM1→3, \mathbb{P}^3 solution

blade/end-walls junctions. The different behavior of the two models also resulted in quite different distributions of total pressure losses close to the end-walls.

Ongoing work focuses on the assessment of the influence of near-wall grid spacing on the turbulent quantities profiles and on a in-depth investigation of the accuracy of the method by looking at several characteristic flow quantities.

ACKNOWLEDGMENTS

This work has been carried out within the EU FP7 IDIHOM project.

References

- D. N. Arnold, F. Brezzi, B. Cockburn, and D. Marini. Unified analysis of discontinuous Galerkin methods for elliptic problems. *SIAM J. Numer. Anal.*, 39(5):1749–1779, 2002.
- S. Balay, K. Buschelman, W. D. Gropp, D. Kaushik, M. G. Knepley, L. C. McInnes, B. F. Smith, and H. Zhang. PETSc Web page, 2001. <http://www.mcs.anl.gov/petsc>.
- F. Bassi and S. Rebay. High-order accurate discontinuous finite element solution of the 2D Euler equations. *J. Comput. Phys.*, 138:251–285, 1997.
- F. Bassi, S. Rebay, G. Mariotti, S. Pedinotti, and M. Savini. A high-order accurate discontinuous finite element method for inviscid and viscous turbomachinery flows. In R. Decuyper and G. Dibelius, editors, *Proceedings of the 2nd European Conference on Turbomachinery Fluid Dynamics and Thermodynamics*, pages 99–108, Antwerpen, Belgium, March 5–7 1997. Technologisch Instituut.
- F. Bassi, A. Crivellini, S. Rebay, and M. Savini. Discontinuous Galerkin solution of the Reynolds-averaged Navier-Stokes and k - ω turbulence model equations. *Comput. & Fluids*, 34:507–540, 2005.
- F. Bassi, A. Ghidoni, S. Rebay, and P. Tesini. High-order accurate p -multigrid discontinuous Galerkin solution of the Euler equations. *Int. J. Numer. Meth. Fluids*, 60(8):847–865, 2009.
- F. Bassi, L. Botti, A. Colombo, A. Crivellini, N. Franchina, A. Ghidoni, and S. Rebay. Very high-order accurate discontinuous Galerkin computation of transonic turbulent flows on aeronautical configurations. In Norbert Kroll, Heribert Bieler, Herman Deconinck, Vincent Couaillier, Harmen van der Ven, and Kaare Sørensen, editors, *ADIGMA - A European Initiative on the Development of Adaptive Higher-Order Variational Methods for Aerospace Applications*, volume 113 of *Notes on Numerical Fluid Mechanics and Multidisciplinary Design*, pages 25–38. Springer Berlin / Heidelberg, 2010a. URL http://dx.doi.org/10.1007/978-3-642-03707-8_3.
- F. Bassi, A. Colombo, N. Franchina, A. Ghidoni, and S. Rebay. Robust and efficient implementation of very high-order discontinuous Galerkin methods in cfd. In Norbert Kroll, Heribert Bieler, Herman Deconinck, Vincent Couaillier, Harmen van der Ven, and Kaare Sørensen, editors, *ADIGMA - A European Initiative on the Development of Adaptive Higher-Order Variational Methods for Aerospace Applications*, volume 113 of *Notes on Numerical Fluid Mechanics and Multidisciplinary Design*, pages 287–299. Springer Berlin / Heidelberg, 2010b. URL http://dx.doi.org/10.1007/978-3-642-03707-8_20.
- F. Bassi, L. Botti, A. Colombo, A. Ghidoni, and S. Rebay. Discontinuous Galerkin for turbulent flows. In Z. J. Wang, editor, *Adaptive high-order methods in computational fluid dynamics*, volume 2 of *Advances in Computational Fluid Dynamics*. World Scientific, 2011a. ISBN 978-981-4313-18-6. URL <http://www.worldscibooks.com/mathematics/7792.html>.

- F. Bassi, N. Franchina, A. Ghidoni, and S. Rebay. Spectral p -multigrid discontinuous Galerkin solution of the Navier-Stokes equations. *International Journal for Numerical Methods in Fluids*, 67 (11):1540–1558, 2011b. ISSN 1097-0363. doi: 10.1002/flid.2430.
- F. Bassi, A. Colombo, A. Ghidoni, and S. Rebay. Simulation of the transitional flow in a low pressure gas turbine cascade with a high-order discontinuous Galerkin method. *Accepted to ASME Journal of Fluids Engineering*, 2012.
- F. Brezzi, G. Manzini, D. Marini, P. Pietra, and A. Russo. Discontinuous Galerkin approximations for elliptic problems. *Numer. Methods Partial Differential Equations*, 16:365–378, 2000.
- D. Hänel, R. Schwane, and G. Seider. On the accuracy of upwind schemes for the solution of the Navier–Stokes equations. AIAA Paper 87-1105 CP, AIAA, 1987.
- H. Hoheisel. Entwicklung neuer Entwurfskonzepte für zwei Turbinengitter, Teil III, Ergebnisse T106. Technical report, Institut für Entwurfsaerodynamik, Braunschweig, 1981.
- K. Lodefier and E. Dick. Modelling of unsteady transition in low-pressure turbine blade flows with two dynamic intermittency equations. *Flow, Turbulence and Combustion*, 76:103–132, 2005.
- F. Menter, A. Garbaruk, and Y. Egorov. Explicit algebraic reynolds stress models for anisotropic wall-bounded flows. In *EUCASS-3rd, European Conference for Aerospace Sciences*, July 6-9th 2009.
- R. D. Stieger and H. P. Hodson. The transition mechanism of highly loaded low-pressure turbine blades. *J. Turbomach.*, 126(4):536–543, 2004.
- R. D. Stieger and H. P. Hodson. The unsteady development of a turbulent wake through a downstream low-pressure turbine blade passage. *J. Turbomach.*, 127(2):388–394, 2005.
- S. Wallin and A. V. Johansson. An explicit algebraic Reynolds stress model for incompressible and compressible turbulent flows. *J. Fluid Mech.*, 403:89–132, 2000.
- D. C. Wilcox. *Turbulence Modelling for CFD*. DCW industries Inc., La Cañada, CA 91011, USA, 1993.